

See discussions, stats, and author profiles for this publication at: <https://www.researchgate.net/publication/6766497>

Evaluating the Roles of the Heme a Side Chains in Cytochrome c Oxidase Using Designed Heme Proteins †

ARTICLE *in* BIOCHEMISTRY · NOVEMBER 2006

Impact Factor: 3.02 · DOI: 10.1021/bi060565t · Source: PubMed

CITATIONS

19

READS

23

6 AUTHORS, INCLUDING:



Amit R Reddi

Johns Hopkins University

14 PUBLICATIONS 401 CITATIONS

SEE PROFILE



Behzad Khodaverdian

University of Utah

2 PUBLICATIONS 34 CITATIONS

SEE PROFILE



Brian R Gibney

City University of New York - Brooklyn College

78 PUBLICATIONS 2,925 CITATIONS

SEE PROFILE

Evaluating the Roles of the Heme *a* Side Chains in Cytochrome *c* Oxidase Using Designed Heme Proteins[†]

Jinyou Zhuang,[‡] Amit R. Reddi,[‡] Zhihong Wang,^{§,||} Behzad Khodaverdian,[§] Eric L. Hegg,^{*,§,||} and Brian R. Gibney^{*,‡}

Department of Chemistry, Columbia University, 3000 Broadway, MC 3121, New York, New York 10027, and
Department of Chemistry, University of Utah, 315 South 1400 East, Salt Lake City, Utah 84112

Received March 21, 2006; Revised Manuscript Received August 7, 2006

ABSTRACT: Heme *a* is a redox cofactor unique to cytochrome *c* oxidases and vital to aerobic respiration. Heme *a* differs from the more common heme *b* by two chemical modifications, the C-8 formyl group and the C-2 hydroxyethylfarnesyl group. The effects of these porphyrin substituents on ferric and ferrous heme binding and electrochemistry were evaluated in a designed heme protein maquette. The maquette scaffold chosen, [Δ7-H3m]₂, is a four-α-helix bundle that contains two bis(3-methyl-L-histidine) heme binding sites with known absolute ferric and ferrous heme *b* affinities. Hemes *b*, *o*, *o*+16, and heme *a*, those involved in the biosynthesis of heme *a*, were incorporated into the bis(3-methyl-L-histidine) heme binding sites in [Δ7-H3m]₂. Spectroscopic analyses indicate that 2 equiv of each heme binds to [Δ7-H3m]₂, as designed. Equilibrium binding studies of the hemes with the maquette demonstrate the tight affinity for hemes containing the C-2 hydroxyethylfarnesyl group in both the ferric and ferrous forms. Coupled with the measured equilibrium midpoint potentials, the data indicate that the hydroxyethylfarnesyl group stabilizes the binding of both ferrous and ferric heme by at least 6.3 kcal/mol via hydrophobic interactions. The data also demonstrate that the incorporation of the C-8 formyl substituent in heme *a* results in a 179 mV, or 4.1 kcal/mol, positive shift in the heme reduction potential relative to heme *o* due to the destabilization of ferric heme binding relative to ferrous heme binding. The two substituents appear to counterbalance each other to provide for tighter heme *a* affinity relative to heme *b* in both the ferrous and ferric forms by at least 6.3 and 2.1 kcal/mol, respectively. These results also provide a rationale for the reaction sequence observed in the biosynthesis of heme *a*.

The integral membrane protein complex cytochrome *c* oxidase (CcO)¹ (E.C. 1.9.3.1) is the terminal enzyme in the energy-transducing, electron-transfer chain in all plants, animals, aerobic yeasts, and some bacteria (1–5). A vital component of aerobic metabolism, CcO catalyzes the four electron–four proton reduction of dioxygen to water along with the concomitant pumping of as many as four protons (eight charge equivalents) across the inner mitochondrial

membrane (6–10). Cytochrome *c* oxidases contain two redox centers, a binuclear Cu_A site and a bis-histidine-ligated heme *a*, that serve as an electron-transfer chain between water-soluble cytochrome *c* and the active site of CcO (1–3, 11). The electrons delivered by cytochrome *c* are shuttled to the buried heterobimetallic catalytic center composed of a high-spin, monohistidine coordinated heme *a*₃ and the Cu_B ligated by three histidines as shown in Figure 1. The heme *a* prosthetic group is unique to terminal oxidases and is biosynthetically derived from heme *b* (protoheme) using two enzymes as shown in Figure 2. First, heme *b* is transformed into heme *o* by converting the vinyl group at C-2 into a hydroxyethylfarnesyl group by heme *o* synthase (12–15). Second, heme *a* synthase oxidizes the methyl group at C-8 on heme *o* to a formyl group to produce heme *a* (15–19). An alcohol intermediate, heme *o*+16, has been isolated in the conversion of heme *o* into heme *a* (19, 20). Despite the importance of the heme *a* prosthetic group, relatively little is known about the role of the C-2 hydroxyethylfarnesyl and C-8 formyl side chains of heme *a* in the electron transfer and dioxygen reduction activity of CcO (15).

Our approach to clarifying the structure–function relationships in natural heme proteins such as CcO is to evaluate the equilibrium thermodynamics of heme affinity and electrochemistry in simplified *de novo* designed heme proteins, or heme protein maquettes (21). By measuring the

[†] This work was supported by an American Heart Association grant to B.R.G. (0455900T) and a National Institutes of Health grant to E.L.H. (GM 66236). A.R.R. acknowledges receipt of a National Science Foundation GK-12 Fellowship (DGE-02-31875).

* Corresponding author. E-mail: brg@chem.columbia.edu. Phone: (212) 854-6346. Fax: (212) 932-1289. For questions concerning heme isolation, synthesis, purification, or characterization, contact erichegg@msu.edu.

[‡] Columbia University.

[§] University of Utah.

^{||} Current address: Department of Biochemistry and Molecular Biology, Michigan State University, 510 Biochemistry Building, East Lansing, MI 48824-1319.

¹ Abbreviations: CcO, cytochrome *c* oxidase; H3m, 3-methyl-L-histidine; TFA, trifluoroacetic acid; ESI/MS, electrospray ionization mass spectrometry; Fmoc, 9-fluorenylmethoxycarbonyl; 'Boc, *tert*-butoxycarbonyl; PAL-PEG-PS, peptide amide linker–polyethylene glycol–polystyrene; HATU, *O*-(7-azabenzotriazol-1-yl)tetramethyluronium; *O*'Bu, *tert*-butyl ester; Trt, trityl; Pmc, 2,2,5,7,8-pentamethylchroman-6-sulfonyl; HPLC, high-performance liquid chromatography; *E*_{m8}, midpoint reduction potential at pH 8.0; SHE, standard hydrogen electrode; Fe(DADPIX), iron diacetyldeuteroporphyrin IX.

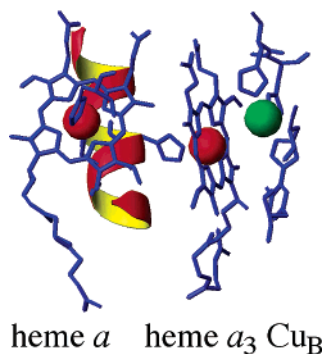


FIGURE 1: Active site structure of bovine cytochrome *c* oxidase showing the heme *a*, heme *a*₃, and Cu_B redox centers. The iron ions are represented by red spheres, and the copper ion is represented by a green sphere. The figure was prepared with MOLMOL (54).

absolute thermodynamic affinity of designed proteins for ferric and ferrous hemes along with the related electrochemistry, we are elucidating the fundamental factors that govern the reduction potentials of hemes in biology (22). We have designed a stably-folded four- α -helix bundle, [$\Delta 7$ -His]₂ or [$\Delta 7$ -H₁₀I₁₄I₂₁]₂, and measured the absolute ferric and ferrous heme *b* affinities for its two bis-His heme binding sites (22). The heme *b*–[$\Delta 7$ -His]₂ maquette displays spectroscopic properties similar to those of natural bis-His coordinated *b*-type cytochromes, e.g., cyt *b*₅. Using a variety of non-natural amino acid ligands in a heme protein maquette, we have explored the effects of ligand basicity on ferric and ferrous heme affinities and found that the more basic 3-methyl-L-histidine had a slightly tighter heme affinity than L-histidine (23, 24). Additionally, we have demonstrated that electron-withdrawing substituents on porphyrins elevate heme reduction potentials by destabilizing the ferric heme with no alteration in ferrous heme affinity for a designed bis-imidazole protein (25).

In this paper, we report the spectroscopic, thermodynamic, and electrochemical consequences of the C-2 farnesyl and C-8 formyl groups of heme *a* in a designed heme protein maquette scaffold. The [$\Delta 7$ -H3m]₂ maquette scaffold, which contains two bis(3-methyl-L-histidine) heme binding sites, was chosen for this study because its absolute affinity for ferric and ferrous heme *b* has been determined and it binds heme *b* more tightly than does the histidine maquette, [$\Delta 7$ -His]₂ (25). In order to separate the contributions of the C-2 farnesyl group from those of the C-8 formyl moiety, the series of hemes involved in the natural biosynthesis of heme *a* (heme *b*, heme *o*, heme *o*+16, and heme *a*) have been incorporated into this maquette scaffold. The affinity of the maquette scaffold for each heme in both the ferric and ferrous forms was measured and correlated with the related electrochemistry. On the basis of the thermodynamic relationship between the equilibrium midpoint reduction potential and the dissociation constants for the ferric and ferrous hemes, we demonstrate that one role of the C-2 hydroxyethylfarnesyl chain is to stabilize the binding of the heme macrocycle to the hydrophobic protein core by at least 6.3 kcal/mol in both the ferric and ferrous oxidation states. We also show that one role of the C-8 formyl group is to raise the midpoint reduction potential of the bound iron by 179 mV, or 4.1 kcal/mol. The enhanced affinity due to the farnesyl tail for the

protein interior counterbalances the weakened ferric heme affinity for the axial ligands due to the electronic effect of the formyl group at C-8.

MATERIALS AND METHODS

Materials. Isolation of heme *a* was performed as previously described (19). Heme *b* (ferriprotoporphylin IX chloride) was purchased from Alfa Aesar. Fmoc-protected amino acids were acquired from Applied Biosystems (Framingham, MA) with the exception of Fmoc-L-H3m-OH, which was purchased from Bachem (King of Prussia, PA). All other chemicals were obtained from Fisher Scientific, VWR, or Sigma-Aldrich-Fluka unless otherwise noted.

Expression of Heme *o* Synthase. The gene encoding for heme *o* synthase in *Bacillus subtilis* (*ctaB*) was cloned into *Escherichia coli* BL21(DE3) pLysS cells as previously described (20). Overnight cultures prepared from single colonies were used to inoculate (1:100 dilution) 500 mL of LB media containing 25 mg/L chloramphenicol and 50 mg/L ampicillin in 2 L indented flasks. Alternatively, overnight cultures were used to inoculate 15 L of LB media (1:50 dilution) in a 19 L Bellco Bioreactor System (O₂ rate of 4 L/min). In both cases, cells were grown to an OD₆₀₀ of 1.2 (measured on an HP 8453 diode array UV–visible spectrophotometer), induced with 75 mg/L isopropyl β -D-1-thiogalactopyranoside (IPTG) for 1–2 h, washed with a 0.25 M sucrose solution, and stored at –80 °C.

Isolation and Purification of Heme *o*. To isolate heme *o*, the cells were thawed and resuspended in 10 mL of distilled water and 30 mL of a 5% HCl–acetone solution (per liter of culture). The cells were sonicated, vortexed vigorously (3 \times 30 s), and then incubated at room temperature for 10 min. The mixture was then diluted with 10 mL of distilled water (per liter of culture), mixed, and clarified by centrifugation at 4400g for 15 min. Heme analysis of the supernatant indicated a heme *b*:heme *o* ratio of approximately 30:70 as determined by HPLC (20). To purify the heme *o*, the supernatant was loaded in 5 mL portions onto a Waters Sep-Pak Vac C18 cartridge (12 cm³ g) that was preequilibrated with 15 mL of 25:75 CH₃CN–H₂O (0.1% trifluoroacetic acid). After loading, the cartridge was washed with an additional 15 mL of 25:75 CH₃CN–H₂O (0.1% TFA) followed by 80:20 CH₃CN–H₂O (0.1% TFA) until all of the heme *b* was eluted (approximately 25–50 mL/L of cell culture). Purified heme *o* was eluted from the column with DMSO (5 mL/L of cell culture), lyophilized, and stored at –80 °C.

Chemical Reduction of Heme *a* to Heme *o*+16. The C-8 aldehyde group on heme *a* was anaerobically reduced to an alcohol under basic conditions using a procedure modified from Vanderkooi et al. (26). In short, HPLC-purified heme *a* (in 60% CH₃CN–40% H₂O–0.1% TFA) was mixed with an equal volume of 50 mM NaOH in 20% pyridine, capped, and sparged with N₂. This solution was then incubated anaerobically with excess dithionite and NaBH₄ for 20 min, followed by the addition of HCl to adjust the pH to 3. The reduced heme *a* was purified from the final solution by reversed-phase HPLC. The identity of the purified heme *o*+16 was confirmed by UV–visible spectroscopy and ESI/MS (20), lyophilized, and stored at –80 °C.

Chemical Synthesis of Peptides. General Procedure. The peptide was synthesized on a continuous flow Applied

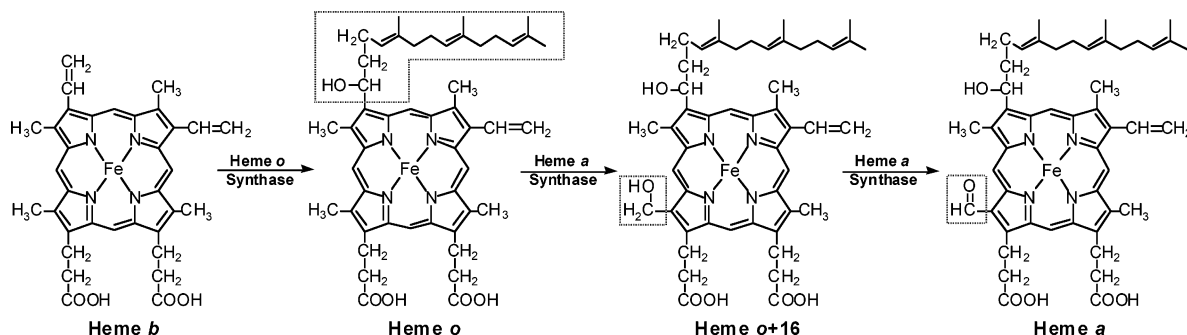


FIGURE 2: Chemical structures of each heme used in this study and their relationship to the heme *a* biosynthetic pathway.

Biosystems Pioneer solid-phase peptide synthesizer using the Fmoc/Bu protection strategy with PAL-PEG-PS resin at 0.2 mmol scale (27). Single-coupling cycles of 30 min with HATU-activation chemistry were employed for all amino acids. The following side chain protecting groups were used: 'Boc (Lys); O'Bu (Glu); Trt (Cys); Pmc (Arg). After peptide assembly, the N-terminus was manually acetylated with acetic anhydride followed by thorough washing with DMF, MeOH, and CH_2Cl_2 . The peptide was cleaved from the resin and simultaneously deprotected using 90:8:2 (v/v/v) trifluoroacetic acid–ethanedithiol–water for 3 h. The crude peptide was precipitated and washed with cold ether, followed by dissolution in water [0.1% (v/v) TFA] and lyophilization. The peptide was purified by reversed-phase C_{18} HPLC using aqueous acetonitrile gradients containing 0.1% (v/v) TFA. The N-terminal cysteine residues of the purified peptide were air-oxidized to the symmetric disulfides in 100 mM ammonium carbonate buffer, pH 9.5 (4–7 h), which was followed by analytical HPLC. The resulting di- α -helical disulfide-bridged peptide was identified with matrix-assisted laser desorption mass spectrometry (MALDI-MS).

UV–Visible Spectroscopy. UV–visible spectra were recorded on Varian Cary 100 and Perkin-Elmer Lambda 25 spectrophotometers using quartz cells of 1.0 and 10 cm path length. Peptide concentrations were determined spectrophotometrically using ϵ_{280} of $5600 \text{ M}^{-1} \text{ cm}^{-1}$ per helix (28).

Heme Affinity Studies. Ferric Heme. Freshly prepared DMSO solutions of heme *b*, heme *o*, heme *o*+16, or heme *a* were added in 0.1 equiv aliquots to peptide solutions (20 mM KPi , 100 mM KCl, pH 8.0). The concentration of the stock solutions was determined using the pyridine–hemochrome method which involves formation of the bis-pyridine ferrous heme complex in basic solution (29). Heme *b* equilibrated within 5 min while hemes *o*, *o*+16, and *a* required 2 h of equilibration between additions. The dissociation constant values were obtained from fitting the absorbance at $\lambda_{\text{max}}^{\text{ox}}$ plotted against [heme]/[four-helix bundle] with a nonlinear least-squares routine in Kaleda-graph (Synergy Software, Reading, PA).

$$\text{Abs}_{\text{meas}} = \text{Abs}_0 + \epsilon_b l [\text{HP}] + \epsilon_f l ([\text{H}_t] - [\text{HP}]) \quad (1)$$

$$[\text{HP}] = \frac{K_d + [\text{P}_t] + [\text{H}_t] - \sqrt{(-K_d - [\text{P}_t] - [\text{H}_t])^2 - (4[\text{P}_t][\text{H}_t])}}{2} \quad (2)$$

The absorbance measured, Abs_{meas} , is a sum of the initial

absorbance, Abs_0 , and the absorbance due to bound heme, $\epsilon_b l [\text{HP}]$, and free heme, $\epsilon_f l ([\text{H}_t] - [\text{HP}])$, where $[\text{H}_t]$ and $[\text{HP}]$ are the concentrations of total heme added and heme protein complex (bound heme), respectively, ϵ_b and ϵ_f are the extinction coefficients of bound and free heme, respectively, l is the path length of the cuvette, K_d is the conditional equilibrium dissociation constant of the heme–peptide complex, and $[\text{P}_t]$ is the total peptide concentration (30). The values of the bound extinction coefficients were determined by converting each heme protein into the corresponding bis-pyridine hemochrome complex.

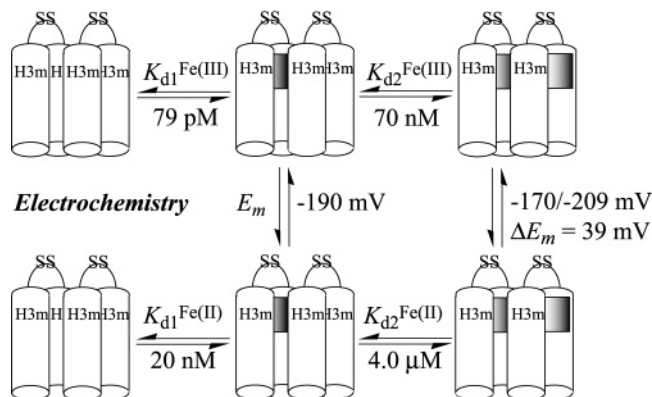
After the spectrum of the oxidized and reduced heme protein was recorded in a 1.0 cm cuvette, the sample was diluted into a 0.1 N solution of NaOH containing 20% (v/v) pyridine and sodium dithionite. The spectrum of the pyridine hemochrome thus produced was recorded and the concentration of the heme was determined using the reported extinction coefficients of the heme *b*, heme *o*, and heme *a* pyridine hemochromes (29). These heme concentrations and the dilution factor between the original heme protein maquette sample and the pyridine hemochrome were used to determine the extinction coefficient of each bound heme, ϵ_b , for use in the data analysis. Since the pyridine hemochrome of heme *o*+16 is not known, the values for heme *o* were used on the basis of the spectra similarity of their maquette complexes. Titrations of each heme into aqueous buffer without peptide present were performed to determine their free heme extinction coefficients, ϵ_f . The slope of the resulting absorbance vs concentration curves yields the extinction coefficients of the unbound hemes which were used in the nonlinear least-squares fitting analysis of heme affinity.

Heme Affinity Studies. Ferrous Heme. Freshly prepared DMSO solutions of heme *b* and heme *o* were added in 0.06 equiv aliquots through a septum into anaerobic peptide solutions (20 mM KPi , 100 mM KCl, pH 8.0). Heme *o* was allowed to equilibrate for 2 h between additions. The samples were maintained at a reducing potential by the addition of sodium dithionite prior to the start of the titration. Due to the length of a typical heme *o* titration (78 h), the spectrophotometer was placed in an AtmosBag (Sigma-Aldrich-Fluka, Milwaukee, WI) under a nitrogen atmosphere to ensure an anaerobic atmosphere. Initial attempts to measure the individual $K_{d1}^{\text{Fe(II)}}$ and $K_{d2}^{\text{Fe(II)}}$ values used 1.0 cm cuvettes, before 10 cm cuvettes were employed in an attempt to measure these tight values. The K_d values were obtained from fitting the absorbance at $\lambda_{\text{max}}^{\text{red}}$ plotted against [heme]/[four-helix bundle] according to eq 1.

Redox Potentiometry. Chemical redox titrations were performed in a 1.0 cm path length anaerobic cuvette equipped

Scheme 1: Thermodynamic Analysis of Heme *b*–[$\Delta 7$ -H3m]₂ Electrochemistry and Heme Affinity

Ferric Heme *b* Dissociation Constants



Ferrous Heme *b* Dissociation Constants

with a platinum working and a calomel reference electrode at 22 °C (31). Ambient redox potentials (measured against the standard hydrogen electrode) were adjusted by addition of aliquots ($<1 \mu\text{L}$) of sodium dithionite or potassium ferricyanide. Titrations were performed on a 3–5 μM four- α -helix bundle containing 0.8 equiv of heme in 20 mM KP_i and 100 mM KCl, pH 8.0; thus only the reduction potentials of maquettes containing a single heme were determined. Electrode solution mediation was facilitated by the following mediators at 10 μM concentration: benzyl viologen, 2,6-dihydroxyanthroquinone, 2-hydroxy-1,4-naphthoquinone, anthroquinone-2-sulfonate, duroquinone, phenazine ethosulfate, phenazine methosulfate, pyocyanine, 1,4-benzoquinone, 1,2-naphthoquinone, and 1,4-naphthoquinone. After equilibration at each potential, the optical spectrum was recorded. Reduction of the hemes was followed by the increase in the Soret band absorption at 420 or 440 nm relative to a baseline point (750 nm). Spectral intensity was plotted against potential, and the data were fit to a single Nernst equation with $n = 1.0$ (fixed).

RESULTS

Experimental Design. The midpoint reduction potential of heme bound to a protein, $E_{m(\text{bound})}$, is governed by the ratio of ferric and ferrous heme dissociation constants, $K_d^{\text{Fe(III)}}/K_d^{\text{Fe(II)}}$, and the reduction potential of the unbound heme, $E_{m(\text{free})}$, as follows (32):

$$E_{m(\text{bound})} = E_{m(\text{free})} + (RT/nF) \ln[K_d^{\text{Fe(III)}}/K_d^{\text{Fe(II)}}] \quad (3)$$

We have been measuring the electrochemistry and the *absolute* affinities of hemes for designed proteins in an effort to clarify the factors that contribute to ferric and ferrous heme affinity and are responsible for the 1000 mV range observed in natural heme protein reduction potentials (33). To this end, we have developed a truncated heme–protein maquette scaffold, [$\Delta 7$ -H3m]₂, that contains two bis(3-methyl-L-histidine) heme binding sites whose absolute affinities of both the ferric and ferrous heme *b* can be accurately measured (25). As shown in Scheme 1, ferric heme *b* binds to [$\Delta 7$ -H3m]₂ more tightly than ferrous heme *b*; i.e., the ratio of $K_d^{\text{Fe(III)}}/K_d^{\text{Fe(II)}}$ is 79 pM/20 nM or 3.9×10^{-3} (25). Since $\Delta\Delta G = -RT \ln(K_d^{\text{Fe(III)}}/K_d^{\text{Fe(II)}})$, the 3.9×10^{-3} ratio of

$K_d^{\text{Fe(III)}}/K_d^{\text{Fe(II)}}$ values represents a 3.3 kcal/mol difference in the ferric and ferrous K_d values (34). Alternatively, this 3.3 kcal/mol $\Delta\Delta G$ value can be expressed as a 142 mV difference between $E_{m(\text{bound})}$ and $E_{m(\text{free})}$, because 1.0 kcal/mol is equal to 43 mV at 25 °C and $n = 1$ due to the relationship $\Delta\Delta G = -nF\Delta E_m$ (34). Thus, the measured –190 mV reduction potential value of heme *b*–[$\Delta 7$ -H3m]₂ indicates that $E_{m(\text{free})}$ has a value of –48 mV and suggests that a bis-His heme protein which binds both ferric and ferrous heme equivalently, i.e., $K_d^{\text{Fe(III)}}$ is equal to $K_d^{\text{Fe(II)}}$, would also have an E_m value of –48 mV.

The ability to determine the *absolute* affinity of the [$\Delta 7$ -H3m]₂ and the related bis-histidine [$\Delta 7$ -His]₂ maquette for heme *b* in both oxidation states along with the coupled electrochemistry is relatively rare among both natural and designed heme proteins, most are only assayed in the ferric state where the subnanomolar K_d values cannot be measured accurately by direct means (35–37). In the case of natural heme protein scaffolds, full thermodynamic analysis is often complicated by tight heme binding or other biochemical issues, e.g., kinetic trapping of the heme moiety (38, 39). The [$\Delta 7$ -H3m]₂ maquette was chosen for the current study based on our ability to measure its ferric and ferrous heme K_d values (22). In addition, only a single heme was incorporated into the maquette scaffold to avoid complications due to heme–heme steric and electrostatic interactions in the data interpretation.

In this study, we evaluate the affinity and electrochemistry of the [$\Delta 7$ -H3m]₂ maquette scaffold (shown schematically in Scheme 1 for heme *b*) for the various hemes in the biosynthetic pathway from heme *b* to heme *a* in both the ferric and ferrous forms. Thermodynamic data from heme *b* and heme *o* are used to evaluate the roles of the C-2 hydroxyethylfarnesyl tail in heme *o* binding and electrochemistry. A comparison of heme *o*, heme *o*+16, and heme *a* binding and electrochemistry yields insight into the effect of successive oxidation of the C-8 methyl group to a formyl group. These data are used to deduce the individual contributions of the farnesyl group and formyl group to ferric and ferrous heme *a* affinity and electrochemistry, as well as to provide insight into the reaction sequence in the biosynthetic pathway of heme *a* (15).

Heme–Peptide Assembly. Figure 3 shows the UV–visible spectra of both ferric and ferrous heme *b*, heme *o*, heme *o*+16, and heme *a* bound to the [$\Delta 7$ -H3m]₂ protein scaffold. The sharp and blue-shifted Soret bands in the optical spectra demonstrate that each heme binds to the designed bis-imidazole heme binding sites in the protein studied because unbound hemes aggregate and yield broad Soret bands. The details of the spectra are listed in Table 1. The optical spectra of hemes *b*, *o*, and *o*+16 bound to the maquettes are very similar, with Soret bands at 408–412 nm in the ferric state and Soret bands at 420–427 nm in the ferrous state. The presence of distinct α/β bands in the spectra of ferrous hemes *b*, *o*, and *o*+16 demonstrates bis-imidazole coordination to the low-spin heme iron in these maquettes, as designed. The spectra of these hemes bound to [$\Delta 7$ -H3m]₂ are reminiscent of those observed for other low-spin bis-His heme *b* proteins, e.g., cyt *b*₅ (40). As anticipated, the electron-withdrawing formyl substituent has a marked effect on the resulting optical spectra of the heme *a* protein maquette. The optical spectra of heme *a* in [$\Delta 7$ -H3m]₂ show Soret bands that are at 420

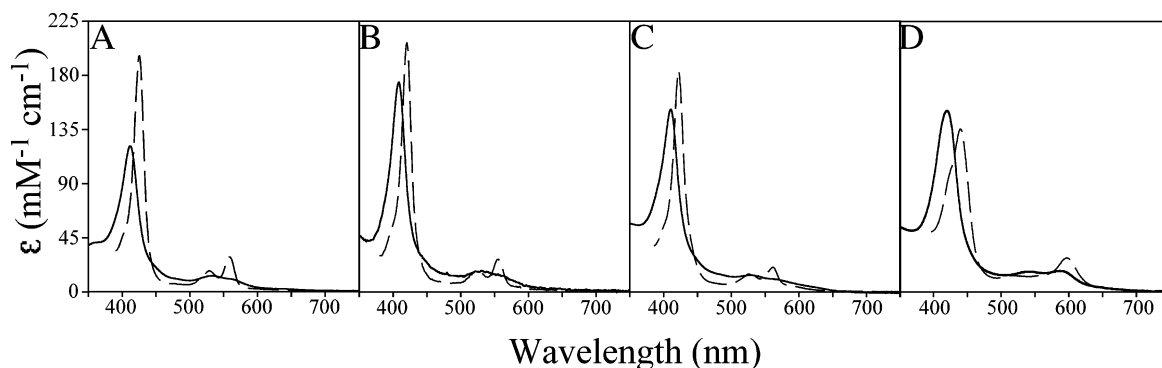


FIGURE 3: UV-visible spectra of (A) heme *b*–[Δ7-H3m]₂, (B) heme *o*–[Δ7-H3m]₂, (C) heme *o*+16–[Δ7-H3m]₂, and (D) heme *a*–[Δ7-H3m]₂ in the ferric (solid line) and ferrous (broken line) states. All experiments were performed at pH 8.0 with 1 μM protein in 20 mM KPi and 100 mM KCl.

Table 1: Spectroscopic and Thermodynamic Characterization of the Heme Protein Maquettes Studied

	ferric			ferrous			<i>E</i> _{m8} (mV) vs SHE
	Soret λ _{max} [ε (mM ^{−1} cm ^{−1})]	<i>K</i> _{d1} ^{Fe(III)}	<i>K</i> _{d2} ^{Fe(III)}	Soret λ _{max} [ε (mM ^{−1} cm ^{−1})]	<i>K</i> _{d1} ^{Fe(II)}	<i>K</i> _{d2} ^{Fe(II)}	
heme <i>b</i>	412 (123)	79 pM	70 nM	427 (191)	20 nM	4 μM	−190
heme <i>o</i>	408 (176)	<0.1 nM	<0.1 nM	420 (205)	<0.1 nM	<0.1 nM	−212
heme <i>o</i> +16	410 (136)	<0.1 nM	<0.1 nM	420 (180)	<0.1 nM ^a	<0.1 nM ^a	−184
heme <i>a</i>	420 (131)	<0.1 nM	<0.1 nM	439 (120)	<0.1 nM ^a	<0.1 nM ^a	−33

^a Estimated on the basis of eq 3 and the measured *K*_{d1}^{Fe(III)} and *K*_{d2}^{Fe(III)} values.

nm in the ferric state and 439 nm in the ferrous state with molar absorptivity values of 131 and 120 mM^{−1} cm^{−1}, respectively. These ferric and ferrous heme *a* maquette spectra are quite similar to those of previous heme *a* maquettes as well as the spectral properties of hemes *a* + *a*₃ in CcO (41, 42).

Ferric Heme–Peptide Binding and Dissociation Constants. UV-visible spectrophotometric titrations were used to determine the two individual ferric heme dissociation constant values, *K*_{d1}^{Fe(III)} and *K*_{d2}^{Fe(III)}, for each heme bound to the [Δ7-H3m]₂ protein scaffold. The evaluated *K*_d^{Fe(III)} values necessitated measurements over a broad peptide concentration range from 50 nM to 1 μM using cuvettes of 1–10 cm path length.

Titration of ferric heme *o* or heme *o*+16 into aqueous solutions of [Δ7-H3m]₂ (20 mM KPi, 100 mM KCl, pH 8.0) results in an increase in the Soret maximum at 408 or 410 nm, consistent with heme binding. Figure 4A illustrates the ferric heme *o* titration of [Δ7-H3m]₂ at 50 nM observed using the Soret band maximum of 408 nm, which demonstrates the binding of two hemes per four-helix bundle with first and second dissociation constant values, *K*_{d1}^{Fe(III)} and *K*_{d2}^{Fe(III)}, tighter than 0.1 nM. Figure 4B shows the related titration of heme *o*+16 into 50 nM [Δ7-H3m]₂ that also evinces the binding of two heme *o*+16 cofactors with both *K*_{d1}^{Fe(III)} and *K*_{d2}^{Fe(III)} values tighter than 0.1 nM, as shown in the inset. The incorporation of heme *a* into [Δ7-H3m]₂ results in a Soret maximum at 420 nm indicative of heme *a* binding as shown in Figure 4C. Similar to the observations for ferric heme *o* and ferric heme *o*+16, the titration of ferric heme *a* into [Δ7-H3m]₂ at 50 nM concentration also shows two hemes binding with *K*_{d1}^{Fe(III)} and *K*_{d2}^{Fe(III)} values tighter than 0.1 nM (inset to Figure 4C). Previously reported heme *a* protein maquettes also possess *K*_d^{Fe(III)} values at the tight-binding limit (41). A comparison of these results with the

*K*_{d2}^{Fe(III)} value of 70 nM reported for heme *b*–[Δ7-H3m]₂ reveals that the heme *a* substituents stabilize porphyrin binding by at least 700-fold, or 3.9 kcal/mol (25).

Ferrous Heme–Peptide Binding and Dissociation Constants. Anaerobic UV-visible spectrophotometric titrations were used to measure the reduced heme dissociation constant values, *K*_{d1}^{Fe(II)} and *K*_{d2}^{Fe(II)}, for heme *b* and heme *o* bound to the [Δ7-H3m]₂ protein scaffold. As with the ferric heme dissociation constant measurements, the *K*_d^{Fe(II)} values required measurements over a broad peptide concentration range from 50 nM to 5 μM using cuvettes of 0.1–10 cm path length.

Titration of ferrous heme *o* into aqueous solutions of [Δ7-H3m]₂ (20 mM KPi, 100 mM KCl, pH 8.0) results in an increase in the Soret maximum at 420 nm, consistent with heme binding. The inset of Figure 5 demonstrates that [Δ7-H3m]₂ at 50 nM concentration binds two heme *o* molecules with dissociation constant values, *K*_{d1}^{Fe(II)} and *K*_{d2}^{Fe(II)}, tighter than 0.1 nM. The ferric *K*_d values and the reduction potentials of heme *o*+16–[Δ7-H3m]₂ and heme *a*–[Δ7-H3m]₂ (vide infra) indicate that the ferrous *K*_d values are too tight to accurately measure, so UV-visible titrations of ferrous heme *o*+16 and ferrous heme *a* into [Δ7-H3m]₂ were not conducted. The available *K*_{d1}^{Fe(II)} and *K*_{d2}^{Fe(II)} data show that ferrous heme *o* binds to the [Δ7-H3m]₂ maquette considerably more tightly than does heme *b* with *K*_{d1}^{Fe(II)} and *K*_{d2}^{Fe(II)} values of 20 nM and 4 μM, respectively, as shown in Scheme 1 (25). Thus, the ferrous dissociation constant data for heme *o* show that the C-2 hydroxyethylfarnesyl tail stabilizes ferrous porphyrin binding by at least 40000-fold, or 6.3 kcal/mol (25).

Heme Redox Potentiometry. The electrochemical equilibrium midpoint reduction potential of each iron porphyrin in [Δ7-H3m]₂ was determined by monitoring the changes in the α, β, and γ bands of the heme absorption spectra as a

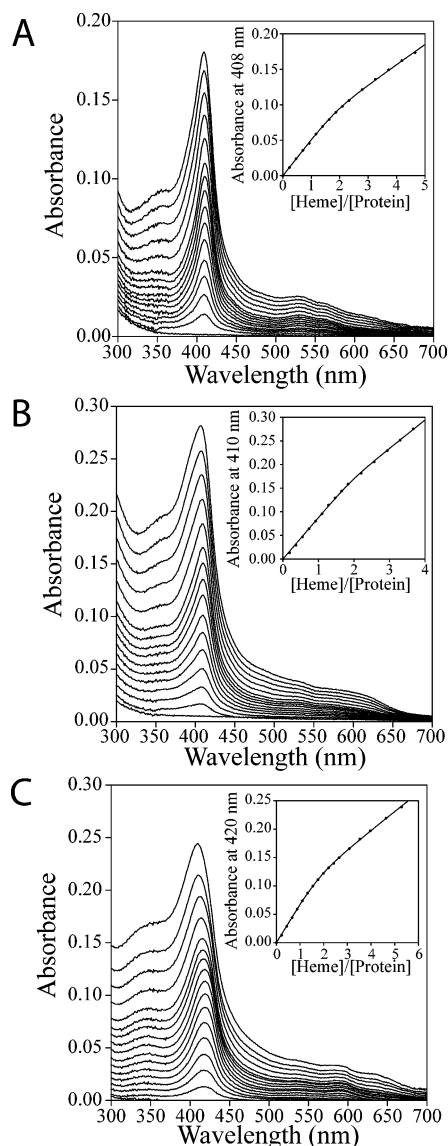


FIGURE 4: Determination of the dissociation constants for ferric (A) heme *o*, (B) heme *o*+16, and (C) heme *a* in $[\Delta 7\text{-H3m}]_2$ at 50 nM four- α -helix bundle concentration (20 mM KPi , 100 mM KCl, pH 8.0). The data for each are fit to a 2:1 heme:protein binding model. The binding curves (insets) indicate tight 2:1 binding of ferric heme *o*, heme *o*+16, and heme *a* to $[\Delta 7\text{-H3m}]_2$.

function of solution potential. Since the midpoint reduction potential of diheme maquettes contains contributions due to heme–heme electrostatics, only the reduction potentials of the heme maquettes containing a single heme were measured for comparison (21, 43). Figure 6 shows the spectroelectrochemistry data for each heme in the maquette scaffold $[\Delta 7\text{-H3m}]_2$. The measured midpoint potential values (E_{m8}) at pH 8.0 for hemes *b*, *o*, *o*+16, and *a* in $[\Delta 7\text{-H3m}]_2$ are -190 ± 8 , -212 ± 8 , -184 ± 8 , and -33 ± 8 mV vs SHE, respectively. The midpoint reduction potential of heme *o* is only slightly lower, 22 mV or 0.5 kcal/mol, than that of heme *b*, which shows that the ratio of the ferric and ferrous K_d values has not changed dramatically between these two hemes. The midpoint potentials of the C-8 modified hemes, heme *o*+16 and heme *a*, are more positive than heme *o*, which indicates that the ratio of the ferric and ferrous K_d values has changed between these hemes (31). Taken together, the redox data sets indicate that conversion of the

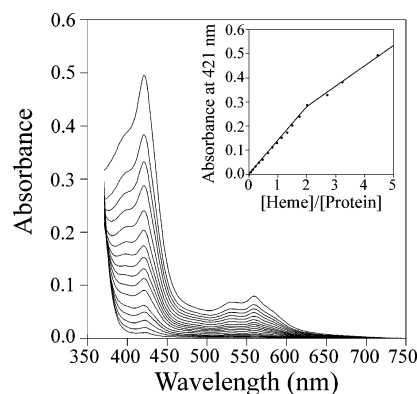


FIGURE 5: Determination of the dissociation constants for ferrous heme *o* in $[\Delta 7\text{-H3m}]_2$ at 50 nM four- α -helix bundle concentration (20 mM KPi , 100 mM KCl, pH 8.0) under strictly anaerobic conditions. Spectra with 0.06, 0.12, 0.21, 0.34, 0.46, 0.65, 0.80, 0.93, 1.12, 1.31, 1.49, 1.74, 2.00, 2.70, 3.22, and 4.44 equiv of heme *o* added per four-helix bundle are shown. The data in the inset are fit to a 2:1 heme:protein binding model with dissociation constant values of less than 0.1 nM.

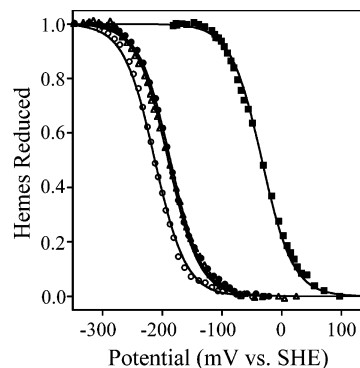


FIGURE 6: Measurement of the electrochemistry of each heme bound to the $[\Delta 7\text{-H3m}]_2$ heme protein maquette. Data for heme *b*– $[\Delta 7\text{-H3m}]_2$ (filled circles), heme *o*– $[\Delta 7\text{-H3m}]_2$ (empty circles), heme *o*+16– $[\Delta 7\text{-H3m}]_2$ (empty triangles), and heme *a*– $[\Delta 7\text{-H3m}]_2$ (filled squares) are shown. Each data set was collected at pH 8.0 under anaerobic conditions at 500 nM protein concentration in 20 mM KPi and 100 mM KCl and fit to a single Nernst equation with $n = 1$ (fixed).

vinyl group at C-2 into a hydroxyethylfarnesyl side chain (heme *o*) does not substantially alter the midpoint reduction potential of the iron but that oxidation of the C-8 methyl to an aldehyde (heme *a*) results in a significantly more positive reduction potential of the bound iron. The difference between heme *b* and heme *a* redox activity in this maquette, 157 mV or 3.6 kcal/mol, is similar to the 174 mV (or 4.0 kcal/mol) difference measured in a larger heme *a* maquette, $[\text{H10A24}]_2$ (41). Furthermore, the value is close to the 140 mV positive shift in E_m observed upon conversion of a *c*-type heme vinyl group in *Thermus thermophilus* cytochrome c_{552} into a formyl group (44).

DISCUSSION

Using a designed heme–protein maquette scaffold, we have delineated the functional roles of the heme *a* side chains in cytochrome *c* oxidase. The spectroscopic properties and electrochemistry of each heme intermediate involved in the heme *a* biosynthetic pathway were determined using the maquette scaffold, $[\Delta 7\text{-H3m}]_2$, with a single heme incorporated. The affinity of the maquette for each iron porphyrin,

heme *b*, heme *o*, heme *o*+16, and heme *a*, was systematically evaluated to elucidate the roles of the side chains in heme function. A comparison of the equilibrium thermodynamics of these hemes in both ferric and ferrous oxidation states reveals the disparate roles of the farnesyl and formyl substituents on heme *a* in CcO. Furthermore, the data provide insight into the reaction order in the biosynthetic pathway from the ubiquitous heme *b* to the rare heme *a* cofactor.

The comparison of the data on heme *b* and heme *o* most clearly demonstrates the influence of the C-2 hydroxyethylfarnesyl chain on heme affinity for the maquette. The $K_{d1}^{\text{Fe(III)}}$ and $K_{d1}^{\text{Fe(II)}}$ values for heme *b*—[$\Delta 7\text{-H3m}$]₂, 79 pM and 20 nM, respectively, are the tightest ferric and ferrous dissociation constants that have been accurately determined for a de novo designed heme protein to date (25). The ratio of these values, $K_{d1}^{\text{Fe(III)}}/K_{d1}^{\text{Fe(II)}}$ or 3.9×10^{-3} , is critical to setting the equilibrium midpoint reduction potential value of -190 mV vs SHE, as described by eq 3. The similarity of the reduction potentials of heme *b* and heme *o* bound to [$\Delta 7\text{-H3m}$]₂, -190 and -212 mV, respectively, indicates that the $K_{d1}^{\text{Fe(III)}}/K_{d1}^{\text{Fe(II)}}$ ratio of heme *o* is 1.7×10^{-3} , only 2.4-fold lower than that observed for heme *b*. Thus, the addition of the hydroxyethylfarnesyl tail does not preferentially stabilize or destabilize the binding of either the ferric or ferrous heme oxidation state to the maquette relative to each other by more than a 0.5 kcal/mol. Therefore, while the $K_{d1}^{\text{Fe(III)}}/K_{d1}^{\text{Fe(II)}}$ ratios between heme *b* and heme *o* are nearly the same, the absolute values of $K_{d1}^{\text{Fe(III)}}$ and $K_{d1}^{\text{Fe(II)}}$ change significantly upon addition of the C-2 hydroxyethylfarnesyl tail. The weak limit of the $K_{d2}^{\text{Fe(II)}}$ value for heme *o*, 0.1 nM, is at least 40000-fold, or >6.3 kcal/mol, tighter than the measured heme *b* $K_{d2}^{\text{Fe(II)}}$ value of $4.0 \mu\text{M}$ (25). Since the $K_{d1}^{\text{Fe(III)}}/K_{d1}^{\text{Fe(II)}}$ ratio of heme *o* is 2.4-fold lower than for heme *b*, the corresponding ferric $K_{d2}^{\text{Fe(III)}}$ value for heme *o* must be at least 96000-fold tighter, or greater than 6.8 kcal/mol. Thus, the hydroxyethylfarnesyl tail stabilizes binding of heme *o* by at least 6.3 kcal/mol in both oxidation states but does not significantly stabilize one heme oxidation state over the other. The observed stabilization of heme *o* binding to the maquette is likely due to the increased hydrophobicity of the porphyrin macrocycle and its partition into the low-dielectric, hydrophobic core of the maquette scaffold. These results mirror the finding of Warncke et al. that the addition of three isoprene units, i.e., a farnesyl tail, increases the quinone binding affinity for the Q_A and Q_B sites of the photosynthetic reaction center protein from *Rhodobacter sphaeroides* by 6.0 kcal/mol (45).

The electrochemical comparison of heme *o* and heme *a* most effectively illustrates the influence of the C-8 formyl group in heme *a*. The presence of the C-8 formyl group raises the midpoint reduction potential of the iron in heme *a* by 179 mV, or 4.1 kcal/mol, relative to heme *o*, which has a methyl group at C-8. A similar 140 mV elevation in the heme E_m value is observed in *T. thermophilus* cytochrome *c*₅₅₂ upon incorporation of a formyl group (44). The elevated reduction potential increases the $K_{d1}^{\text{Fe(III)}}/K_{d1}^{\text{Fe(II)}}$ ratio by 1130-fold, 4.1 kcal/mol, for heme *a* relative to heme *o*. In other words, ferric heme *a* is destabilized relative to ferrous heme *a* by 1130-fold more than ferric heme *o* is destabilized relative to ferrous heme *o*. While the heme binding data for heme *o* and heme *a* do not directly reveal the absolute values for

their individual $K_{d1}^{\text{Fe(III)}}$ and $K_{d1}^{\text{Fe(II)}}$ values, based on the value of 1.7×10^{-3} for the $K_{d1}^{\text{Fe(III)}}/K_{d1}^{\text{Fe(II)}}$ ratio of heme *o*, the $K_{d1}^{\text{Fe(III)}}/K_{d1}^{\text{Fe(II)}}$ ratio of heme *a* can be estimated to be 1.9, or 1.7×10^{-3} times 1130. Thus, the ferrous heme *a* is estimated to bind only 1.9-fold more tightly than ferric heme *a* to the bis-imidazole sites in [$\Delta 7\text{-H3m}$]₂ due to the relative destabilization of ferric heme *a* binding with respect to ferrous heme *a*. A similar situation was observed when heme *b* in [$\Delta 7\text{-H3m}$]₂ was replaced with iron diacetyldeuteroporphyrin IX [Fe(DADPIX)], which has acetyl groups in the place of the heme *b* vinyl groups. Fe(DADPIX) was observed to bind [$\Delta 7\text{-H3m}$]₂ with a $K_{d1}^{\text{Fe(III)}}$ value of 200 nM and $K_{d1}^{\text{Fe(II)}}$ value of 37 nM, which resulted in a midpoint reduction potential value of -30 mV vs SHE (25). Thus, ferrous Fe(DADPIX) bound 5.4-fold, or 1.0 kcal/mol, more tightly to [$\Delta 7\text{-H3m}$]₂ than ferric Fe(DADPIX). The electron-withdrawing acetyl groups on Fe(DADPIX) elevated the iron midpoint reduction potential by 160 mV, 3.7 kcal/mol, relative to heme *b* in [$\Delta 7\text{-H3m}$]₂. In relative terms, the similarity in the Fe(DADPIX)—[$\Delta 7\text{-H3m}$]₂ and heme *a*—[$\Delta 7\text{-H3m}$]₂ midpoint reduction potential values results from similar $K_{d1}^{\text{Fe(III)}}/K_{d1}^{\text{Fe(II)}}$ ratios, 5.4 and 1.9, respectively. In absolute terms, analysis of the heme binding thermodynamics of Fe(DADPIX)—[$\Delta 7\text{-H3m}$]₂ and heme *b*—[$\Delta 7\text{-H3m}$]₂ has shown that the observed 160 mV positive shift in the E_{m8} value of Fe(DADPIX)—[$\Delta 7\text{-H3m}$]₂ is due almost solely to the destabilization of the ferric state with little alteration of ferrous heme affinity. On the basis of these observations, it is inferred that destabilization of ferric heme *a* binding to the bis-imidazole sites in [$\Delta 7\text{-H3m}$]₂ by the formyl group is responsible for the elevated reduction potential of heme *a* relative to heme *o*. This midpoint potential shift is functionally important in CcO as it allows heme *a* ($E_m = +380$ mV) to accept electrons from cytochrome *c* ($E_m = +260$ mV) (46, 47). The related quinol oxidases from plants utilize heme *o* ($E_m = +200$ mV) and lower potential hydroquinones ($E_m = +70$ mV) as electron donors to dioxygen (48).

The influence of electron-withdrawing groups on ferric heme affinity may also be functionally relevant in *Paracoccus pantotrophus* cytochrome *cd*₁ nitrite reductase, a bifunctional enzyme that is also an oxidase (49, 50). The catalytically inert, oxidized enzyme contains both a bis-His ligated *c*-type cytochrome and a noncovalently bound, His-Tyr coordinated cytochrome *d*₁, a chlorin with peripheral ketone groups. Upon reduction to a catalytically competent state, Tyr25 dissociates to generate a high-potential, five-coordinate heme *d*₁ with a concomitant switch in the *c*-type heme ligands to His-Met. The presence of the electron-withdrawing ketone groups likely facilitates the ligand dissociation reaction by weakening the affinity of the heme *d*₁ for the His-Tyr site. In addition, the lack of either a farnesyl group or cysteine thioethers to anchor heme *d*₁ in the enzyme may also contribute to the fluxionality of heme *d*₁ required to activate the enzyme. Likewise, the thioether linkages may prevent the dissociation of the *c*-type heme upon reduction (51).

These thermodynamic results indicate the disparate roles that the C-2 and C-8 porphyrin substituents play in heme *a* function. One role of the C-2 hydroxyethylfarnesyl tail is to strengthen the affinity of the porphyrin for the protein scaffold in both oxidation states by at least 6.3 kcal/mol without significantly altering the heme electrochemistry. A

role for the C-8 formyl group is to make the reduction potential of the iron more positive by destabilizing the binding of ferric heme relative to ferrous heme by 4.1 kcal/mol, or 179 mV. In thermodynamic terms, the addition of both substituents to heme *b* to form heme *a* results in an increase in ferric affinity by at least 2.1 kcal and an increase in ferrous heme affinity by at least 6.3 kcal/mol. In addition to these roles, Lu and co-workers have recently proposed that the hydroxyl group at C-2 may also be involved in proton delivery to the active site of CcO or in stabilizing the reactive intermediates of the oxygen reduction reaction (52).

Furthermore, these results are consistent with the observed order of peripheral substitution in the biosynthesis of heme *a* from heme *b*. The initial step in the heme *a* biosynthetic pathway involves the addition of the C-2 hydroxyethylfarnesyl group. Conversion of heme *b* into heme *o* by the integral membrane protein heme *o* synthase increases the affinity of the porphyrin for low dielectric media which effectively sequesters the heme *o* product into the cellular membranes. The subsequent conversion of heme *o* into heme *a* by oxidation of the C-8 methyl group by heme *a* synthase shifts the midpoint reduction potential of the heme more positive, making it a better electron acceptor in CcO. If the reaction order was reversed, the oxidation of the C-8 methyl to a formyl group would provide the cell with a water-soluble, high-potential iron porphyrin which might be incorporated into a variety of natural heme *b* binding sites, e.g., cyt *b*₅, myoglobin, and cytochromes P-450. This would affect the activity of a wide variety of heme proteins involved in vital biological processes from dioxygen transport to redox catalysis. By placing the C-2 hydroxyethylfarnesyl group onto the porphyrin first, the biosynthetic pathway prevents the misincorporation of high-potential hemes into water-soluble heme proteins. Thus, the thermodynamic data are consistent with expectations based on the observed order of porphyrin substitution reactions in converting heme *b* into heme *a*.

CONCLUSION

Since the initial isolation of heme *a* from beef heart muscle (53), the consequences of its unique structure on cytochrome *c* oxidase function have been debated (15). The thermodynamic analysis presented herein provides new insights into the impact of the peripheral side chains on heme *a* in CcO structure and function. Data from all of the hemes involved in the heme *a* biosynthetic pathway indicate that a role of the hydroxyethylfarnesyl tail at C-2 in heme *a* is to stabilize the binding of both oxidation states to a bis-imidazole site by at least 6.3 kcal/mol. This stabilization is functionally important because the data show that one effect of the formyl group at C-8 is to destabilize ferric heme *a* binding to the same site by 4.1 kcal/mol. This destabilization results in a 179 mV positive shift in the iron reduction potential which is necessary for CcO function. Lastly, the counterbalancing roles of these substituents provide insight into the biosynthetic pathway of heme *a* which introduces the hydroxyethylfarnesyl chain before the oxidation of the C-8 methyl group.

REFERENCES

1. Abramson, J., Shimamura, T., and Iwata, S. (2004) Structures of bacterial heme-copper oxidases, in *Respiration in Archaea and Bacteria: Diversity of Prokaryotic Electron Transport Carriers* (Zannoni, D., Ed.) pp 115–128, Kluwer Academic Publishers, Dordrecht.
2. Ferguson-Miller, S., and Babcock, G. T. (1996) Heme/copper terminal oxidases, *Chem. Rev.* 96, 2889–2907.
3. Michel, H., Behr, J., Harrenga, A., and Kannt, A. (1998) Cytochrome *c* oxidase: Structure and spectroscopy, *Annu. Rev. Biophys. Biomol. Struct.* 27, 329–356.
4. García-Horsman, J. A., Barquera, B., Rumbley, J., Ma, J., and Gennis, R. B. (1994) The superfamily of heme-copper respiratory oxidases, *J. Bacteriol.* 176, 5587–5600.
5. Thöny-Meyer, L. (1997) Biogenesis of respiratory cytochromes in bacteria, *Microbiol. Mol. Biol. Rev.* 61, 337–376.
6. Bloch, D., Belevich, I., Jasaitis, A., Ribacka, C., Puustinen, A., Verkhovsky, M. I., and Wikström, M. (2004) The catalytic cycle of cytochrome *c* oxidase is not the sum of its two halves, *Proc. Natl. Acad. Sci. U.S.A.* 101, 529–533.
7. Brzezinski, P., Larsson, G., and Ådelroth, P. (2004) Functional aspects of heme-copper terminal oxidases, in *Respiration in Archaea and Bacteria: Diversity of Prokaryotic Electron Transport Carriers* (Zannoni, D., Ed.) pp 129–153, Kluwer Academic Publishers, Dordrecht.
8. Malmström, B. G. (2001) Respiration: cytochrome oxidase, in *Biological Systems and Artificial Supramolecular Systems* (Balzani, V., Ed.) pp 39–55, Wiley-VCH, New York.
9. Namslauer, A., and Brzezinski, P. (2004) Structural elements involved in electron-coupled proton transfer in cytochrome *c* oxidase, *FEBS Lett.* 567, 103–110.
10. Trumpower, B. L., and Gennis, R. B. (1994) Energy transduction by cytochrome complexes in mitochondrial and bacterial respiration: The enzymology of coupling electron transfer reactions to transmembrane proton translocation, *Annu. Rev. Biochem.* 63, 675–716.
11. Carr, H. S., and Winge, D. R. (2003) Assembly of cytochrome *c* oxidase within the mitochondrion, *Acc. Chem. Res.* 36, 309–316.
12. Glerum, D. M., and Tzagoloff, A. (1994) Isolation of a human cDNA for heme *a*:farnesyltransferase by functional complementation of a yeast COX10 mutant, *Proc. Natl. Acad. Sci. U.S.A.* 91, 8452–8456.
13. Puustinen, A., and Wikström, M. (1991) The heme groups of cytochrome *o* from *Escherichia coli*, *Proc. Natl. Acad. Sci. U.S.A.* 88, 6122–6126.
14. Saiki, K., Mogi, T., Ogura, K., and Ankaru, Y. (1993) *In vitro* heme *o* synthesis by the *cyoE* gene product from *Escherichia coli*, *J. Biol. Chem.* 268, 26041–26045.
15. Mogi, T. (2003) Biosynthesis and role of heme *o* and heme *a*, in *The Iron and Cobalt Pigments: Biosynthesis, Structure, and Degradation* (Kadish, K. M., Smith, K. M., and Guillard, R., Eds.) pp 157–181, Academic Press, Amsterdam.
16. Barros, M. H., Carlson, C. G., Glerum, D. M., and Tzagoloff, A. (2001) Involvement of mitochondrial ferredoxin and Cox15p in hydroxylation of heme *o*, *FEBS Lett.* 492, 133–138.
17. Sakamoto, J., Hayakawa, A., Uehara, T., Noguchi, S., and Sone, N. (1999) Cloning of *Bacillus stearothermophilus* *ctaA* and heme *a* synthesis with the CtaA protein produced in *Escherichia coli*, *Biosci. Biotechnol. Biochem.* 63, 96–103.
18. Svensson, B., Lübken, M., and Hederstedt, L. (1993) *Bacillus subtilis* CtaA and CtaB function in haem *a* biosynthesis, *Mol. Microbiol.* 10, 193–201.
19. Brown, K. R., Brown, B. M., Hoagland, E., Manye, C. L., and Hegg, E. L. (2004) Heme *a* synthase does not incorporate molecular oxygen into the formyl group of heme *a*, *Biochemistry* 43, 8616–8624.
20. Brown, K. R., Allan, B. M., Do, P., and Hegg, E. L. (2002) Identification of novel hemes generated by heme *a* synthase: Evidence for two successive monooxygenase reactions, *Biochemistry* 41, 10906–10913.
21. Robertson, D. E., Farid, R. S., Moser, C. C., Urbauer, J. L., Mulholland, S. E., Pidikiti, R., Lear, J. D., Wand, A. J., DeGrado, W. F., and Dutton, P. L. (1994) Design and synthesis of multi-haem proteins, *Nature* 368, 425–432.
22. Reedy, C. J., Kennedy, M. L., and Gibney, B. R. (2003) Thermodynamic characterization of ferric and ferrous haem binding to a designed four- α -helix protein, *Chem. Commun.*, 570–571.
23. Privett, H. K., Reedy, C. J., Kennedy, M. L., and Gibney, B. R. (2002) Nonnatural amino acid ligands in heme protein design, *J. Am. Chem. Soc.* 124, 6828–6829.

24. Zhuang, J., Amoroso, J. H., Kinloch, R., Dawson, J. H., Baldwin, M. J., and Gibney, B. R. (2004) Design of a five-coordinate heme protein maquette: A spectroscopic model of deoxyMyoglobin, *Inorg. Chem.* 43, 8218–8220.
25. Zhuang, J., Amoroso, J. H., Kinloch, R., Dawson, J. H., Baldwin, M. J., and Gibney, B. R. (2006) Evaluation of electron-withdrawing group effects on heme binding in a designed protein: Implications for heme *a* in cytochrome *c* oxidase, *Inorg. Chem.* 45, 4685–4694.
26. Vanderkooi, G., and Stotz, E. (1965) Reductive alteration of heme *a* hemochromes, *J. Biol. Chem.* 240, 3418–3424.
27. Kates, S. A., and Albericio, F. (2000) *Solid-Phase Synthesis: A Practical Guide*, p 826, Marcel Dekker, New York.
28. Fasman, G. D. (1976) *Handbook of Biochemistry and Molecular Biology, Proteins*, 1, 3rd ed., CRC Press, Boca Raton, FL.
29. Berry, E. A., and Trumpower, B. L. (1987) Simultaneous determination of hemes *a*, *b*, and *c* from pyridine hemochrome spectra, *Anal. Biochem.* 161, 1–15.
30. Price, N. C., and Dwek, R. A. (1979) *Principles and Problems in Physical Chemistry for Biochemists*, 2nd ed., Oxford University Press, Oxford.
31. Dutton, P. L. (1978) Redox potentiometry: determination of midpoint potentials of oxidation-reduction components of biological electron-transfer systems, *Methods Enzymol.* 54, 411–435.
32. Nasset, M. J. M., Shokhirev, N. V., Enemark, P. D., Jacobson, S. E., and Walker, F. A. (1996) Models of the cytochromes. Redox properties and thermodynamic stabilities of complexes of “hindered” iron(III) and iron(II) tetraphenylporphyrinates with substituted pyridines and imidazoles, *Inorg. Chem.* 35, 5188–5200.
33. Reedy, C. J., and Gibney, B. R. (2004) Heme protein assemblies, *Chem. Rev.* 104, 589–604.
34. Bard, A. J., and Faulkner, L. R. (2001) *Electrochemical Methods. Fundamentals and Applications*, 2nd ed., p 833, John Wiley & Sons, New York.
35. Lombardi, A., Nasti, F., and Pavone, V. (2001) Peptide-based heme protein models, *Chem. Rev.* 101, 3165–3190.
36. Lu, Y., Berry, S. M., and Pfister, T. D. (2001) Engineering novel metalloproteins: Design of metal-binding sites into native protein scaffolds, *Chem. Rev.* 101, 3047–3080.
37. Xu, Z., and Farid, R. S. (2001) Design, synthesis and characterization of a novel hemoprotein, *Protein Sci.* 10, 236–249.
38. Hargrove, M. S., Barrick, D., and Olson, J. S. (1996) The association rate constant for heme binding to globin is independent of protein structure, *Biochemistry* 35, 11293–11299.
39. Silchenko, S., Sippel, M. L., Kuchment, O., Benson, D. R., Mauk, A. G., Altuve, A., and Rivera, M. (2000) Hemin is kinetically trapped in cytochrome *b₅* from rat outer mitochondrial membrane, *Biochem. Biophys. Res. Commun.* 273, 467–472.
40. Rivera, M., Barillas-Mury, C., Christensen, K. A., Little, J. W., Wells, M. A., and Walker, F. A. (1992) Gene synthesis, bacterial expression and ¹H NMR spectroscopic studies on the rat outer mitochondrial membrane cytochrome *b₅*, *Biochemistry* 31, 12233–12240.
41. Gibney, B. R., Isogai, Y., Reddy, K. S., Rabanal, F., Grosset, A. M., Moser, C. C., and Dutton, P. L. (2000) Self-assembly of heme *a* and heme *b* in a designed four-helix bundle. Implications for a cytochrome *c* oxidase maquette, *Biochemistry* 39, 11041–11049.
42. Yonetani, T. (1961) Studies on cytochrome oxidase. III. Improved preparation and some properties, *J. Biol. Chem.* 236, 1850–1856.
43. Shifman, J. M., Gibney, B. R., Sharp, R. E., and Dutton, P. L. (2000) Heme redox potential control in *de novo* designed four- α -helix bundle proteins, *Biochemistry* 39, 14813–14821.
44. Fee, J. A., Todaro, T. R., Luna, E., Sanders, D., Hunsicker-Wang, L. M., Patel, K. M., Bren, K. L., Gomez-Moran, E., Hill, M. G., Ai, J., Loehr, T. M., Oertling, W. A., Williams, P. A., Stout, C. D., McRee, D., and Pastuszyn, A. (2004) Cytochrome *rC₅₅₂*, formed during expression of the truncated, *Thermus thermophilus* cytochrome *c₅₅₂* gene in the cytoplasm of *Escherichia coli*, reacts spontaneously to form protein-bound 2-formyl-4-vinyl (*Spirographis*) heme, *Biochemistry* 43, 12162–12176.
45. Warncke, K., Gunner, M. R., Braun, B. S., Gu, L., Yu, C.-A., Bruce, J. M., and Dutton, P. L. (1994) Influence of hydrocarbon tail structure on quinone binding and electron-transfer at the Q_A and Q_B sites in the photosynthetic reaction center protein, *Biochemistry* 33, 7830–7841.
46. Tsudzuki, T., and Wilson, D. F. (1971) The oxidation-reduction potentials of the hemes and copper of cytochrome oxidase from beef heart, *Arch. Biochem. Biophys.* 145, 149–154.
47. Myer, Y. P., Saturno, A. F., Verma, B. C., and Pande, A. (1979) Horse heart cytochrome *c*. The oxidation-reduction potential and protein structures, *J. Biol. Chem.* 254, 11202–11207.
48. Schultz, B. E., and Chan, S. I. (1998) Thermodynamics of electron transfer in *Escherichia coli* cytochrome *bo₃*, *Proc. Natl. Acad. Sci. U.S.A.* 95, 11643–11648.
49. Fülöp, V., Moir, J. W. B., Ferguson, S. J., and Hajdu, J. (1995) The anatomy of a bifunctional enzyme: Structural basis for reduction of oxygen to water and synthesis of nitric oxide by cytochrome *cd₁*, *Cell* 81, 369–377.
50. Williams, P. A., Fülöp, V., Garman, E. F., Saunders, N. F. W., Ferguson, S. J., and Hajdu, J. (1997) Haem-ligand switching during catalysis in crystals of a nitrogen-cycle enzyme, *Nature* 389, 406–412.
51. Cowley, A. B., Lukat-Rodgers, G. S., Rodgers, K. R., and Benson, D. R. (2004) A possible role for the covalent heme-protein linkage in cytochrome *c* revealed via comparison of N-acetylmicroperoxidase-8 and a synthetic, monohistidine-coordinated heme peptide, *Biochemistry* 43, 1656–1666.
52. Wang, N., Zhao, X., and Lu, Y. (2005) Role of heme types in heme-copper oxidases: Effects of replacing a heme *b* with a heme *o* mimic in an engineered heme-copper center in myoglobin, *J. Am. Chem. Soc.* 127, 16541–16547.
53. Warburg, O., and Gewitz, H. S. (1951) Cytohemins from the heart muscle, *Z. Physiol. Chem.* 288, 1–4.
54. Koradi, R., Billeter, M., and Wüthrich, K. (1996) MOLMOL: a program for display and analysis of macromolecular structures, *J. Mol. Graphics* 14, 51–55.

BI060565T